

# Super-Earths in the TW Hya disc

Daniel Mentiplay<sup>1\*</sup>, Daniel J. Price<sup>1</sup> and Christophe Pinte<sup>1,2</sup>

<sup>1</sup>*Monash Centre for Astrophysics (MoCA) and School of Physics and Astronomy, Monash University, Clayton Vic 3800, Australia*

<sup>2</sup>*Univ. Grenoble Alpes, CNRS, IPAG, F-38000 Grenoble, France*

## ABSTRACT

We test the hypothesis that the sub-millimetre thermal emission and scattered light gaps seen in recent observations of TW Hya are caused by planet-disc interactions. We perform global three-dimensional dusty smoothed particle hydrodynamics simulations, comparing synthetic observations of our models with dust thermal emission, CO emission and scattered light observations. We find that the dust gaps observed at 24 au and 41 au can be explained by two super-Earths ( $\sim 4 M_{\oplus}$ ). A planet of approximately Saturn-mass can explain the CO emission and the depth and width of the gap seen in scattered light at 94 au. Our model produces a prominent spiral arm while there are only hints of this in the data. To avoid runaway growth and migration of the planets we require a disc mass of  $\lesssim 10^{-2} M_{\odot}$  in agreement with CO observations but 10–100 times lower than the estimation from HD line emission.

**Key words:** protoplanetary discs — planet-disc interactions — hydrodynamics — stars: individual (TW Hydrae) — submillimetre: planetary systems — infrared: planetary systems

## 1 INTRODUCTION

TW Hya, our nearest gas-rich protoplanetary disc, was recently imaged by ALMA at 870  $\mu\text{m}$  (Andrews et al. 2016). These observations of thermal emission from  $\sim 100 \mu\text{m}$  dust in the midplane show a series of stunning axisymmetric gaps. At just 60 pc (Gaia Collaboration et al. 2018) TW Hya presents a unique opportunity to observe planet formation on our doorstep. Being a member of the 3–20 Myr old (Barrado Y Navascués 2006) TW Hya association means TW Hya is older than the typical disc lifetime of  $\sim 3$  Myr (Haisch et al. 2001) implying that planet formation should almost be complete.

van Boekel et al. (2017) observed TW Hya in polarized scattered light using the Spectro-Polarimetric High-contrast Exoplanet REsearch (SPHERE) instrument on the Very Large Telescope. Scattered light observations trace the small grains in the upper layers of the gas disc. These grains are tightly coupled to the gas via drag. Of the two main gaps in the sub-mm dust emission (at 24 au and 41 au) only the inner gap is observed in the scattered light image.

Estimates of the gas mass in TW Hya vary over several orders of magnitude. Thi et al. (2010) use radiative transfer modelling of CO emission to infer a gas mass  $(0.5\text{--}5) \times 10^{-3} M_{\odot}$ . Whereas Bergin et al. (2013) use hydrogen deuteride (HD) observations to infer a disc mass  $> 0.05 M_{\odot}$ . At this mass the self-gravity of the disc is significant and gravitational instability may lead to disc fragmentation (Kratte & Lodato 2016). Trapman et al. (2017), using additional constraints on the vertical structure from Kama et al. (2016) and adding HD 2–1 line observations, suggest a gas mass, in

between these two extremes, of  $(6\text{--}9) \times 10^{-3} M_{\odot}$ . Recent carbon sulfide (CS) molecular observations find a minimum disc mass of  $3 \times 10^{-4} M_{\odot}$  (Teague et al. 2018).

The characteristic timescale for aerodynamic drag to act on dust grains is determined by the dimensionless stopping time, or Stokes number,  $St$  (Weidenschilling 1977; Takeuchi & Lin 2002). The Stokes number controls the rate of vertical settling and radial drift. The Stokes number is proportional to the grain size and inversely proportional to the gas density. Small grains ( $\sim \mu\text{m}$ ) experience high drag and have low  $St$ . Whereas large grains ( $\gtrsim \text{cm}$ ) are largely decoupled from the gas phase and have high  $St$ . Grains with  $St \sim 1$  experience the greatest rate of settling and drift and lead to the formation of axisymmetric rings (Ayliffe et al. 2012; Dipierro et al. 2015). The different response of small and large grains to gas drag can be used to infer the mechanism for the origin of the gaps.

To reproduce the axisymmetric gaps observed in recent ALMA observations, various mechanisms have been proposed, including: planet-disc interactions (Dipierro et al. 2015), self-induced dust trapping (Gonzalez et al. 2017), vortices (Zhu & Stone 2014), condensation fronts (Zhang et al. 2015), non-ideal MHD effects (Béthune et al. 2016) and zonal flows (Johansen et al. 2009; Flock et al. 2015).

In this Letter, we explore the hypothesis that the axisymmetric rings and gaps in the TW Hya disc are carved by planets. Our approach is similar to Dipierro et al. (2015) who explored a similar hypothesis for HL Tau. We aim to constrain the planet masses required to explain the observational data on TW Hya and to motivate follow up observations.

\* daniel.mentiply@monash.edu

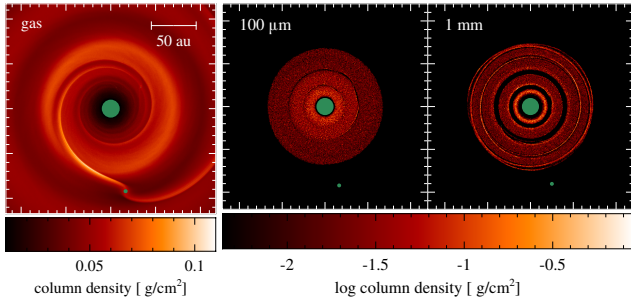


**Figure 1.** Gas (left), 100  $\mu\text{m}$  dust (center), and 1 mm dust (right) surface density for the model with 4  $M_{\oplus}$  inner planets (24 and 41 au) and 0.3  $M_J$  outer planet (94 au) after 29400 years. The green markers are sink particles with radius proportional to accretion radius. We do not model the inner ( $\lesssim 10$  au) disc. The outer edge of the dust disc is  $\sim 70$  au.

## 2 METHODS

### 2.1 Numerical method

We perform 3D global simulations of a dusty gas disc with embedded protoplanets using PHANTOM, a smoothed particle hydrodynamics (SPH) code (Price et al. 2018). Dust interacts with the gas via a drag force. This allows the dust to settle to the midplane and to migrate radially. The dust also interacts gravitationally with the central star and embedded planets. We use a low disc mass, so the disc is not self-gravitating.

We simulate two dust grain sizes in separate calculations: 100  $\mu\text{m}$  grains with  $\text{St} \sim 0.3$  and 1 mm grains with  $\text{St} \sim 3$ . We then combine the results of the 100  $\mu\text{m}$  and 1 mm calculations for radiative transfer post-processing. These grains have Stokes number near unity to ensure efficient settling and radial migration of our simulated grains. In this regime it is appropriate to use the two-fluid method (Laibe & Price 2012). We use  $10^7$  particles for the gas, and  $2.5 \times 10^5$  for the dust. We use a greater number of gas particles to prevent dust becoming trapped under the gas resolution scale (Laibe & Price 2012). For 100  $\mu\text{m}$ - and 1 mm-sized grains, the gas mean free path is large compared with the grain size, and so we assume Epstein drag (Epstein 1924). We assume spherical grains with a material density of  $3 \text{ g cm}^{-3}$ . We also perform gas-only simulations to explore the impact of the outer planet.

We use sink particles (Bate et al. 1995) to represent the central star and three embedded protoplanets. The sink particles interact gravitationally with the disc and with each other. Gravitationally bound dust and gas within the accretion radius is accreted onto the sink. For computational efficiency, we set the stellar accretion radius to be the inner edge of the disc.

### 2.2 Initial conditions

We assume a distance of 59.5 au (Gaia Collaboration et al. 2016) and a stellar mass of  $0.8 M_{\odot}$  (Andrews et al. 2012). Scattered light and CO line observations show that the gas disc extends out to at least  $\sim 200$  au (Thi et al. 2010) so we take the outer edge of the gas disc to be 200 au. We set the inner edge of the disc to be  $R_{\text{in}} = 10$  au for computational efficiency. We do not attempt to model the inner disc ( $\lesssim 10$  au) in this study.

We set up a disc consisting of SPH particles following Lodato & Price (2010). We assume a gas mass of  $7.5 \times 10^{-4} M_{\odot}$  between 10 au and 200 au. Extrapolating to  $R_{\text{in}} \approx 1$  au implies a total disc mass higher by 1–10% depending on the surface density prescription, in the low end of the Thi et al. (2010) range, but above

the Teague et al. (2018) minimum. We set the initial surface density profile as a smoothed power law:  $\Sigma = \Sigma_{\text{in}}(R/R_{\text{in}})^{-p}(1 - \sqrt{R_{\text{in}}/R})$ , where we adopt a shallow surface density profile with  $p = 0.5$ . This, with our gas disc mass, gives a surface density of  $\Sigma \approx 0.05 - 0.08 \text{ g cm}^{-2}$ , corresponding to a Stokes number of  $\text{St} \approx 0.25 - 0.4$  for 100  $\mu\text{m}$  grains.

We assume a vertically isothermal equation of state  $P = [c_s(R)]^2 \rho$  with  $T = 30 \text{ K}(R/R_{\text{in}})^{-0.25}$  where  $c_s^2 = k_B T / \mu m_p$ . This matches the CO snowline (20 K at 19 au) from van't Hoff et al. (2017) together with a midplane temperature of 15 K at 60 au following previous modelling (Andrews et al. 2012). From these we infer a disc aspect ratio of  $H/R = c_s/(\Omega R) = 0.034$  at  $R_{\text{in}}$ . Flaherty et al. (2018) provide an upper limit on the turbulent velocity in the outer disc of  $v_{\text{turb}}/c_s \approx 0.04 - 0.13$ . This corresponds to an  $\alpha \sim (v_{\text{turb}}/c_s)^2 \lesssim 0.002 - 0.02$ . We choose a disc viscosity (Shakura & Sunyaev 1973) at the lower end of this range and set the SPH artificial viscosity to  $\alpha_{\text{AV}} = 0.1$  giving  $\alpha \sim 0.001$ .

The dust disc is more compact than the gas disc. Thermal dust emission shows that the sub-mm dust disc extends to  $\sim 50$  au (Andrews et al. 2016). We set the outer edge of the dust disc to  $R_{\text{out}} = 80$  au, just inside the orbital radius of the outer planet. This is to allow for some radial drift, without having to follow the drift of dust particles from the gas outer radius. We use the same inner edge as for the gas disc. Dust disc mass estimates are in the range  $(2-6) \times 10^{-4} M_{\odot}$  (Calvet et al. 2002; Thi et al. 2010). With our gas disc mass this gives a dust-to-gas ratio of  $\approx 0.25-0.8$  which is one to two orders of magnitude higher than the typical interstellar value. However, TW Hya is an old disc within which we can expect significant evolution away from its initial conditions. We set the dust-to-gas ratio (for 100  $\mu\text{m}$  and for 1 mm grains) to 0.05.

### 2.3 Embedded planets

We assume two super-Earth to super-Neptune mass planets at 24 au and 41 au, respectively, to reproduce the two main observed gaps in sub-mm emission (Andrews et al. 2016). We explored masses in the range of 4–24  $M_{\oplus}$  for these planets. To reproduce the outer gap observed in scattered light (van Boekel et al. 2017) we placed a more massive planet at 94 au. We explored a range of masses for the outer planet between 0.1–2  $M_J$ . We set the planetary accretion radius  $R_{\text{acc}}$  to half the Hill radius,  $R_H = a \sqrt[3]{m_p/3M_*}$ , where  $a$  is the semi-major axis, and  $m_p$  and  $M_*$  are the planet mass and stellar mass, respectively. Accretion proceeds unchecked for particles within 80% of the accretion radius. A possible argument in favour of planets is that the two inner planets are located at a possible 7:3 mean motion resonance where migration may stall due to resonance trapping (Terquem & Papaloizou 2007).

### 2.4 Synthetic observations

We use the 3D radiative transfer code MCFOST (Pinte et al. 2006, 2009) to post-process the PHANTOM output to produce simulated ALMA band 7 images, CO maps and polarized scattered light images. We use a Voronoi (unstructured) mesh using Voro++ (Rycoff 2009) in which the computational domain is subdivided into cells generated from the positions of the SPH gas particles. We assume an inclination of  $5^\circ$  and position angle  $152^\circ$  (Huang et al. 2018) when making synthetic observations of the disc.

Within each cell we split the distribution of dust grain sizes into 100 logarithmic bins from  $0.03 \mu\text{m}$  to 1 mm. Grains smaller than  $1 \mu\text{m}$  are assumed to trace the gas. Grains larger than 100  $\mu\text{m}$

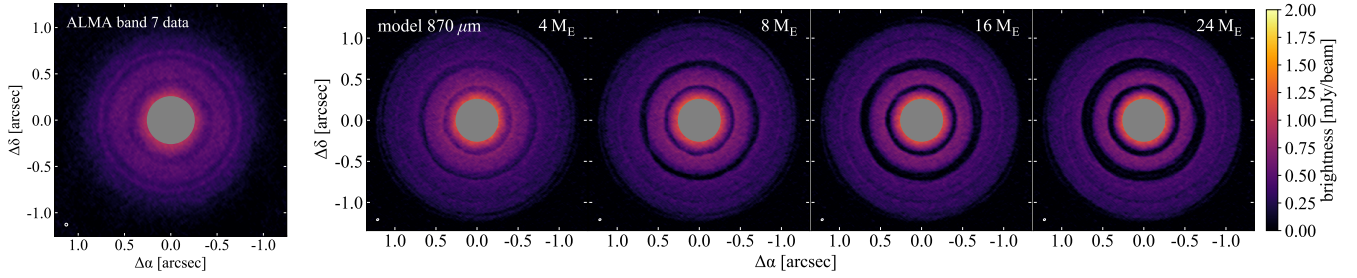


**Figure 2.** Inner planets (24 and 41 au). Synthetic observations of dust thermal emission at  $870\ \mu\text{m}$ , compared with ALMA band 7 observations from [Andrews et al. \(2016\)](#). From left to right: dust+gas models with 4, 8, 16, 24  $M_{\oplus}$  inner planets. The beam has FWHM  $28 \times 21$  mas in the model image, compared with 30 mas FWHM (1.6 au) circular beam in the observations. We obscured the inner  $\approx 15$  au as we did not model that region.

are interpolated between  $100\ \mu\text{m}$  and  $1\ \text{mm}$  simulations. Grains of intermediate size are interpolated between gas and  $100\ \mu\text{m}$  dust. Total dust mass is set to  $2.5 \times 10^{-4}\ M_{\odot}$ . We use  $10^7$  photon packets to determine the temperature and to produce synthetic observations.

We use the Common Astronomy Software Application (CASA) ALMA simulator (version 4.7) to produce synthetic band 7 ALMA images at  $870\ \mu\text{m}$  to compare with [Andrews et al. \(2016\)](#). We use a transit duration of 45 minutes, add thermal noise from the receivers and atmosphere, and set the precipitable water vapour to 0.5 mm. To match the beam size of the observations, we choose an ALMA antenna configuration (cycle 3.8) which gives a beam of FWHM  $28 \times 21$  mas at  $\text{PA} = -60.3^\circ$ .

We post-process gas-only PHANTOM simulations in MCFOST to produce polarized scattered light images, and CO emission maps, assuming the dust follows the gas. In these calculations we assume a dust-to-gas ratio of 0.01. From  $1.6\ \mu\text{m}$  (H-band) scattered light maps we calculated the azimuthal Stokes component  $Q_{\phi}$ , scaled by  $R^2$ . We then we add Gaussian noise and convolve with a Gaussian beam with a FWHM of 48.5 mas, following the H-band SPHERE observations in [van Boekel et al. \(2017\)](#).

We also produce CO emission maps in the  $J = 3-2$  line. We assume  $T_{\text{gas}} = T_{\text{dust}}$  and that the emission is at LTE, as we are looking at low- $J$  CO lines. We assume a CO-to- $\text{H}_2$  molecular abundance of  $10^{-4}$ . We produce channel maps at 0.1 km/s resolution to then calculate the  $M_0$  moment map. We convolve with a Gaussian beam with FWHM of  $139 \times 131$  mas with a  $\text{PA} = -74.9^\circ$  following the ALMA observations presented by [Huang et al. \(2018\)](#).

### 3 RESULTS

Figure 1 shows the gas and dust surface density after 29400 years (250, 100, and 32 orbits of the 24, 41, and 94 au planets, resp.) for the model with 4  $M_{\oplus}$  inner planets (24 and 41 au) and 0.3  $M_J$  outer planet (94 au). The dust disc extends to  $\sim 70$  au (right of Figure 1). We observe cleared dust gaps at the locations of the two inner planets, while the planets are not massive enough to carve gaps in the gas (Figure 1). The Saturn-to-Jupiter-mass outer planet carves a (partial) gap in the gas, and produces a spiral density wave. The region interior to 10 au is devoid of dust merely because it is within the accretion radius of the stellar sink particle.

The inner planets (24 and 41 au) accreted  $\approx 10$ –20% over the simulation time. For models with an initial mass of 4, 8, 16, and 24  $M_{\oplus}$ , the 24 au planet accreted 0.4, 0.9, 1.8, and 2.4  $M_{\oplus}$ , respectively, and the 41 au planet accreted 1.0, 2.0, 3.3, and 4.4  $M_{\oplus}$ , respectively. The outer planet (94 au) accreted 65%, 45%, 20%, and 10% for models with initial mass 0.1, 0.3, 1, and 2  $M_J$ , respectively. Planet migration was negligible.

#### 3.1 Dust thermal emission

Figure 2 compares our synthetic band 7 ALMA observations of dust thermal continuum emission for models with 4, 8, 16, and 24  $M_{\oplus}$  inner planets with the ALMA observations ([Andrews et al. 2016](#)). Low mass planets ( $< 0.1\ M_J \approx 32\ M_{\oplus}$ ) successfully reproduce the width and axisymmetry of the gaps at 24 and 41 au.

Increasing the planet mass increases the gap width, as expected. Each planet mass produces axisymmetric gaps. However, only the 4  $M_{\oplus}$  planet produces a partially cleared gap (like the ALMA observation). This is due to the fact that, at 4  $M_{\oplus}$ , the planet is not large enough to carve a fully opened gap in the  $100\ \mu\text{m}$  dust disc, but it is large enough to do so in the  $1\ \text{mm}$  dust disc. The gap width at both 24 and 41 au is  $\approx 5$  au which is consistent with the ALMA gap widths. However, the 41 au ALMA gap is narrower than the 24 au gap, unlike our model, which suggests that the innermost planet is the more massive of the two. This finding is consistent with the scattered light observations, which show a low contrast gap at 24 au but none at 41 au. A planet mass of 4  $M_{\oplus}$  for the innermost planet is also consistent with an upper limit suggested by [Nomura et al. \(2016\)](#). However, it is not consistent with modelling from [van Boekel et al. \(2017\)](#) following [Duffell & Dong \(2015\)](#), and with the low-viscosity models of [Dong & Fung \(2017\)](#).

#### 3.2 Scattered light and CO emission

Figure 3 (top) compares our synthetic polarized scattered light H-band observations for gas-only models with outer planet masses 0.1, 0.3, 1, and 2  $M_J$  after 102000 years, i.e. 100 orbits at 94 au, with the SPHERE observation from [van Boekel et al. \(2017\)](#). The spiral arm induced by the outer planet is visible in all our synthetic observations. For the 0.3, 1, and 2  $M_J$  we observe a dip in scattered light at the orbital radius of the planet. Figure 4 quantifies this by comparing the azimuthally-averaged brightness profiles. The brightness contrast between the peak and gap for a Saturn mass ( $\approx 0.3\ M_J$ ) planet is consistent with the SPHERE observation. A 0.1  $M_J$  planet, by contrast, fails to reproduce the gap.

Figure 3 (bottom) compares synthetic CO  $J = 3-2$  emission maps for gas-only models with outer planet masses 0.1, 0.3, 1, and 2  $M_J$ , with the ALMA observations ([Huang et al. 2018](#)). The 0.3  $M_J$  model, which best fits the scattered light radial profile, is consistent with CO observations. For a planet larger than 0.3  $M_J$ , the gas surrounding the planet is visible in the  $M_0$  map. This is because our model has infinite signal-to-noise. Gas near the planet has perturbed velocity and emits in a large number of channels. While the signal in each channel is faint and would not be detected by ALMA, when aggregated in the  $M_0$  map, it becomes visible. Higher S/N ALMA observations might be able to detect the planet.



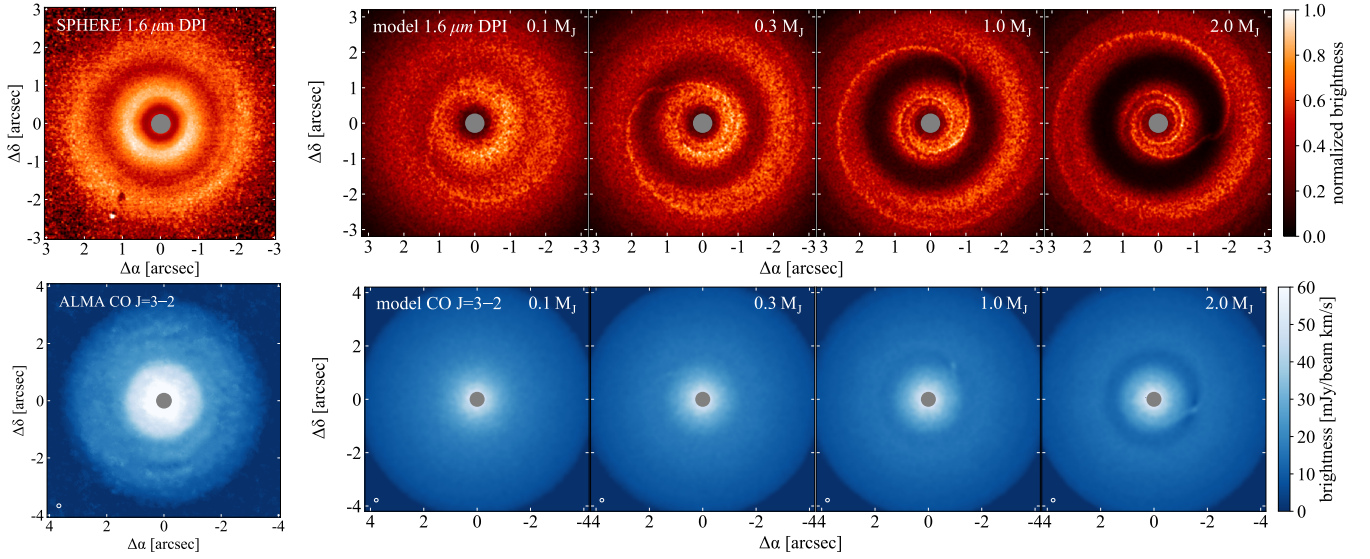


**Figure 3.** Gas-only models with outer planet (94 au) masses 0.1, 0.3, 1, and 2  $M_J$  after 100 orbits at 94 au. *Top:* Comparison of synthetic observations of  $1.6 \mu\text{m}$  polarized intensity scaled by  $R^2$  with the SPHERE observation. We convolved with a circular Gaussian beam of FWHM 48.5 mas, and added noise. *Bottom:* Comparison of synthetic CO  $J = 3-2$  integrated intensity emission maps with the ALMA observation. We convolved with a Gaussian beam of  $139 \times 131$  mas with a PA =  $-74.9^\circ$ . Top left panel is reproduced from [van Boekel et al. \(2017\)](#) and bottom left is from data presented in [Huang et al. \(2018\)](#).

#### 4 DISCUSSION

For computational efficiency we did not model the inner disc (within  $\sim 10$  au). This leads to a hotter temperature at radii  $\gtrsim 20$  au, where the stellar radiation penetrates to the midplane. Thus the dust thermal emission within the innermost planet orbit is larger than the observation. At radii  $> 20$  au, we recover the vertically stratified thermal structure expected for an optically thick disc. This indicates that direct star light is not penetrating the midplane, and that the temperature in this region of the disc does not depend anymore on the details of the inner disc.

The overall flux is consistent to within a factor of 2 of the ALMA observation. The contrast in flux between gaps and rings is  $\approx 25\%$ , greater than the observed contrast of 5–20% ([Andrews et al. 2016](#)). Our model has only two grain sizes in the range that contribute emission in ALMA band 7. Multigrain dust simulations that include a greater range of grain sizes contributing to emission, and calculate the full back reaction of all dust grain sizes on the gas, may alleviate that problem ([Hutchison et al. 2018](#)).

Spectral index observations from [Huang et al. \(2018\)](#) suggest that within the gaps the maximum grain size is at most a few mm, whereas in the bright rings cm grains are present. Therefore, the disc mass may be an order of magnitude higher than our assumed mass, such that mm grains have Stokes number of 100  $\mu\text{m}$  grains in our calculations. For a  $4 M_\oplus$  planet, the gaps would contain mm grains but no cm grains, as inferred from observations ([Huang et al. 2018](#)).

There is a tension between the outer planet mass required to reproduce the gap in scattered light and CO observations, and the mass required to hide a spiral arm. The synthetic observation from the  $0.3 M_J$  model (top of Figure 3) shows a greater degree of azimuthal asymmetry than the SPHERE observation. Models with a lower mass planet ( $\sim 0.1 M_J$ ) are more azimuthally symmetric. However, at those masses we fail to reproduce the gap in both scattered light and in CO emission. A mass of  $0.3 M_J \approx 95 M_\oplus$  is higher than suggested by previous authors ([Dong & Fung 2017](#); [van Boekel et al. 2017](#)). It is possible that our calculations need to

run for longer to reach a steady state gap profile. Figure 5 shows the evolution of azimuthally-averaged surface density. If the gap is not fully opened on the timescale of the simulation then we can only put an upper limit on the planet mass. It is also possible that we are overestimating the planet mass if the gap were accentuated by shadowing from the inner disc ([Debes et al. 2013, 2017](#); [Poutte et al. 2018](#)). The pebble isolation mass ([Bitsch et al. 2018](#)) for 100  $\mu\text{m}$  and 1 mm grains is  $\approx 20 M_\oplus$  which is well below each model presented here. This suggests that inward radial drift of these grains occurred before the planet reached its current mass.

For our disc model, the stellar accretion rate is  $1.5 \times 10^{-10} M_\odot \text{ yr}^{-1}$  which is an order of magnitude below the estimated rate ([Brickhouse et al. 2012](#)). The accretion rate is given by  $\dot{M} = 3\pi \Sigma \alpha c_s H$ . This suggests two modifications to increase  $\dot{M}$ : we could increase the disc mass, and we could increase the disc viscosity. As discussed, a ten-fold increase in disc mass is possible, given spectral index observations. The viscosity is constrained by observations ([Flaherty et al. 2018](#)). An alternative may be that accretion is driven by winds ([Simon et al. 2017](#)).

Increasing the stellar accretion rate via either approach increases the planetary accretion rate. For the  $4 M_\oplus$  model the inner planets (24 and 41 au) accrete  $0.4 M_\oplus$  and  $1.0 M_\oplus$ , respectively, over the  $\approx 30000$  yrs of simulation time. Extrapolating this rate to a million years leads to accretion of  $\sim 10\text{--}30 M_\oplus$ , which is uncomfortably high. Increasing the disc viscosity also requires larger planets to form gaps initially as a greater gravitational torque is required to overcome the viscous torque from the gas ([Dipierro et al. 2016](#)).

The product of planetary mass and accretion rate  $M_p \dot{M}_p$  for the outer planet (94 au) in the  $0.3 M_J$  model is  $2 \times 10^{-7} M_J^2/\text{yr}$ , which is a factor of 5 greater than the upper limit deduced from Keck/NIRC2 vortex coronagraph observations ([Ruane et al. 2017](#)). Given that our model constrains the planet mass via the gap depth this suggests that the accretion rate may be too high in our model. We use a relatively large sink radius for computational reasons. A smaller sink radius may reduce the accretion rate, and improve agreement with the observed value.

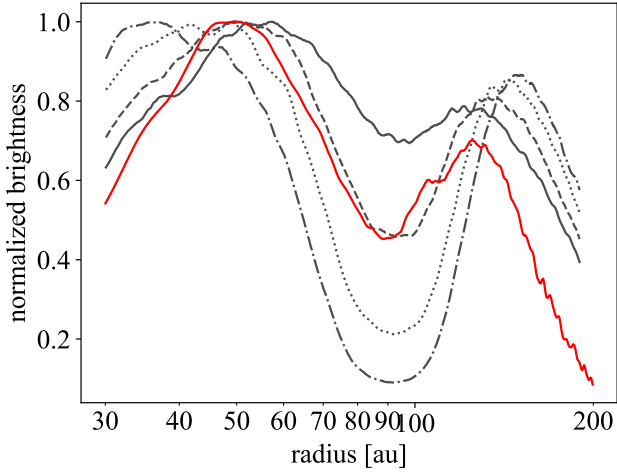


**Figure 4.** Azimuthally-averaged profiles of  $1.6 \mu\text{m}$  polarized intensity scaled by  $R^2$ , normalized to the peak at  $\approx 40\text{--}50$  au. Solid, dashed, dotted, and dot-dashed lines are for  $0.1$ ,  $0.3$ ,  $1$ , and  $2 M_J$  models after 100 orbits at 94 au. Red shows H-band data from van Boekel et al. (2017).

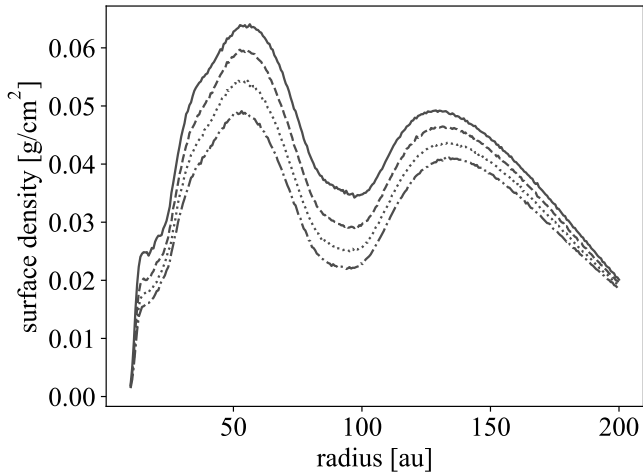


**Figure 5.** Surface density profile for gas-only model with  $0.3 M_J$  planet at 94 au. Top to bottom lines are at 40, 60, 80, and 100 orbits at 94 au.

## 5 SUMMARY

We have performed global three-dimensional SPH simulations of a dusty disc with embedded protoplanets and produced synthetic observations of dust continuum, CO emission, and polarized scattered light to test our model against recent observations.

- (i) We reproduce the gaps in dust emission in the ALMA observations of TW Hya with two  $\approx 4 M_{\oplus}$  planets at 24 au and 41 au.
- (ii) We show that a giant planet ( $0.1\text{--}1.0 M_J$ ) at 94 au can explain the main gap in scattered light observations, and is consistent with CO observations. However, a spiral arm is also evident, for which there is only tentative evidence in the SPHERE image.
- (iii) Our model requires a disc mass  $\lesssim 10^{-2} M_{\odot}$  in agreement with CO observations rather than the  $> 0.05 M_{\odot}$  disc mass inferred by Bergin et al. (2013). A low mass disc is consistent with recent constraints on disc turbulence (Flaherty et al. 2018).

## ACKNOWLEDGEMENTS

DM is funded by a Research Training Program Stipend from the Australian government. We acknowledge Australia Research Council funding via DP180104235, FT130100034, and FT170100040. We used gSTAR and OzStar, funded by Swinburne University of Technology and the Australian government, the MonARCH cluster at Monash, and SPLASH (Price 2007).

## REFERENCES

- Andrews S. M., et al., 2012, *ApJ*, **744**, 162  
 Andrews S. M., et al., 2016, *ApJ*, **820**, L40  
 Ayliffe B. A., Laibe G., Price D. J., Bate M. R., 2012, *MNRAS*, **423**, 1450  
 Barrado Y Navascués D., 2006, *A&A*, **459**, 511  
 Bate M. R., Bonnell I. A., Price N. M., 1995, *MNRAS*, **277**, 362  
 Bergin E. A., et al., 2013, *Nature*, **493**, 644  
 Béthune W., Lesur G., Ferreira J., 2016, *A&A*, **589**, A87  
 Bitsch B., et al., 2018, *A&A*, **612**, A30  
 Brickhouse N. S., et al., 2012, *ApJ*, **760**, L21  
 Calvet N., et al., 2002, *ApJ*, **568**, 1008  
 Debes J. H., Jang-Condell H., Weinberger A. J., Roberge A., Schneider G., 2013, *ApJ*, **771**, 45  
 Debes J. H., et al., 2017, *ApJ*, **835**, 205  
 Dipierro G., et al., 2015, *MNRAS*, **453**, L73  
 Dipierro G., Laibe G., Price D. J., Lodato G., 2016, *MNRAS*, **459**, L1  
 Dong R., Fung J., 2017, *ApJ*, **835**, 146  
 Duffell P. C., Dong R., 2015, *ApJ*, **802**, 42  
 Epstein P. S., 1924, *Physical Review*, **23**, 710  
 Flaherty K. M., et al., 2018, *ApJ*, **856**, 117  
 Flock M., et al., 2015, *A&A*, **574**, A68  
 Gaia Collaboration et al., 2016, *A&A*, **595**, A1  
 Gaia Collaboration et al., 2018, *A&A*, **616**, A1  
 Gonzalez J.-F., Laibe G., Maddison S. T., 2017, *MNRAS*,  
 Haisch Jr. K. E., Lada E. A., Lada C. J., 2001, *ApJ*, **553**, L153  
 Huang J., et al., 2018, *ApJ*, **852**, 122  
 Hutchison M., Price D. J., Laibe G., 2018, *MNRAS*,  
 Johansen A., Youdin A., Klahr H., 2009, *ApJ*, **697**, 1269  
 Kama M., et al., 2016, *A&A*, **588**, A108  
 Kratter K., Lodato G., 2016, *ARA&A*, **54**, 271  
 Laibe G., Price D. J., 2012, *MNRAS*, **420**, 2345  
 Lodato G., Price D. J., 2010, *MNRAS*, **405**, 1212  
 Nomura H., et al., 2016, *ApJ*, **819**, L7  
 Pinte C., Ménard F., Duchêne G., Bastien P., 2006, *A&A*, **459**, 797  
 Pinte C., et al., 2009, *A&A*, **498**, 967  
 Poteet C. A., et al., 2018, *ApJ*, **860**, 115  
 Price D. J., 2007, *PASA*, **24**, 159  
 Price D. J., et al., 2018, *PASA*, **35**, e031  
 Ruane G., et al., 2017, *AJ*, **154**, 73  
 Rycroft C. H., 2009, *Chaos*, **19**, 041111  
 Shakura N. I., Sunyaev R. A., 1973, *A&A*, **24**, 337  
 Simon J. B., Bai X.-N., Flaherty K. M., Hughes A. M., 2017, preprint, ([arXiv:1711.04770](https://arxiv.org/abs/1711.04770))  
 Takeuchi T., Lin D. N. C., 2002, *ApJ*, **581**, 1344  
 Teague R., et al., 2018, *ApJ*, **864**, 133  
 Terquem C., Papaloizou J. C. B., 2007, *ApJ*, **654**, 1110  
 Thi W.-F., et al., 2010, *A&A*, **518**, L125  
 Trapman L., Miotello A., Kama M., van Dishoeck E. F., Bruderer S., 2017, *A&A*, **605**, A69  
 Weidenschilling S. J., 1977, *MNRAS*, **180**, 57  
 Zhang K., Blake G. A., Bergin E. A., 2015, *ApJ*, **806**, L7  
 Zhu Z., Stone J. M., 2014, *ApJ*, **795**, 53  
 van Boekel R., et al., 2017, *ApJ*, **837**, 132  
 van't Hoff M. L. R., Walsh C., Kama M., Facchini S., van Dishoeck E. F., 2017, *A&A*, **599**, A101